

Single-Crystalline Branched Zinc Phosphide Nanostructures: Synthesis, Properties, and Optoelectronic Devices

Rusen Yang,[†] Yu-Lun Chueh,^{†,‡} Jenny Ruth Morber,[†] Robert Snyder,[†]
Li-Jen Chou,[‡] and Zhong Lin Wang^{*,†}

School of Materials Science and Engineering, Georgia Institute of Technology, Atlanta, Georgia 30332-0245, and Department of Materials Science and Engineering, National Tsing Hua University, Hsinchu 300, Republic of China

Received September 21, 2006; Revised Manuscript Received December 9, 2006

ABSTRACT

Hierarchical tree-shaped nanostructures, nanobelts, and nanowires of Zn₃P₂ were synthesized in a thermal assisted laser ablation process. All nanostructures are tetragonal phased Zn₃P₂ with excellent crystallinity and are free from an oxidation layer according to electron microscopy and X-ray diffraction analyses. Optical measurement revealed a strong absorption from the ultraviolet to near-infrared regions. Optoelectronic devices fabricated using individual nanowires demonstrate a high sensitivity and rapid response to impinging light. A crossed heterojunction of an n-type ZnO nanowire and a p-type Zn₃P₂ nanowire has been characterized, and it offers a great potential for a high efficient spatial resolved photon detector.

Being a novel optoelectronic material, Zn₃P₂ has the following advantages over some other materials. It has a direct band gap in the range of 1.4–1.6 eV, which is the optimum range for solar energy conversion. The large optical absorption coefficient ($> 10^4 \text{ cm}^{-1}$) and a long minority diffusion length ($\sim 13 \mu\text{m}$) of Zn₃P₂ permit high current collection efficiency.¹ In addition, the constituent materials are abundant and cheap and would allow the large scale deployment of such devices as solar cells, infrared (IR) and ultraviolet (UV) sensors, lasers, and light polarization step indicators.^{2,3} In order to investigate the potential applications of Zn₃P₂, several kinds of heterojunctions have been designed, such as InP/Zn₃P₂,⁴ Mg/Zn₃P₂,⁵ Zn₃P₂/ZnSe,^{2,6} ITO/Zn₃P₂,⁷ and ZnO/Zn₃P₂.⁸ However, the majority of research on Zn₃P₂ has been limited to thin films, and very little work has been done in the nanoscale range except for very few reports on the synthesis of Zn₃P₂ nanoparticles^{9–11} and on the synthesis of nanotrumpets with an unavoidable ZnO layer coated on the surface.¹² Because of the large excitonic radii, Zn₃P₂ is expected to exhibit pronounced quantum size effect, which has been observed for Zn₃P₂ nanoparticles.¹⁰ To the best of our knowledge, the electric property and photoresponse of Zn₃P₂ nanostructures, and heterojunctions made from Zn₃P₂ nanostructures, have not been reported thus far.

In this paper we report for the first time the synthesis of single crystalline tree-shape Zn₃P₂ structure arrays, nano-

wires, and nanobelts. The morphology and crystal structure were determined by electron microscopy and analytical techniques. In addition, the optical property of the synthesized nanostructures has been measured through photoluminescence (PL). Furthermore, we also present the crossed heterojunction made using a ZnO nanowire and a Zn₃P₂ nanowire. Optoelectronic measurements of single Zn₃P₂ nanowire and the crossed heterojunction indicate that Zn₃P₂ was very sensitive to light and the heterojunction exhibits enhanced performance, which implies that the Zn₃P₂ nanostructures have promising applications in optoelectronics.

Various nanostructures have been synthesized with thermal evaporation¹³ or laser ablation methods.^{14–16} Combining the two techniques, Zn₃P₂ structures were synthesized using a thermal-assisted pulsed laser ablation (TAPLA) process in a single-zone horizontal tube furnace, which is shown schematically in Figure 1. The two ends of the tube were closed and water-cooled to ensure a stable synthesis environment inside. A mixture of 0.8 g of ZnO and 0.12 g of graphite powder was placed in the middle of the tube. In order to transport the source vapor and reduce possible oxidization during the synthesis, N₂ was introduced from one end of the tube at a flow rate of 25 sccm during the entire synthesis process. A cylindrical target containing Zn₃P₂, ZnO, and Zn (in ratios of 2:1:1 by weight) was placed downstream. A single crystalline (111) Si wafer was placed in front of the target, serving as a collecting substrate. In order to minimize the residual oxygen, the tube was first evacuated to 10^{-2}

* Corresponding author. zhong.wang@mse.gatech.edu.

[†] Georgia Institute of Technology.

[‡] National Tsing Hua University.

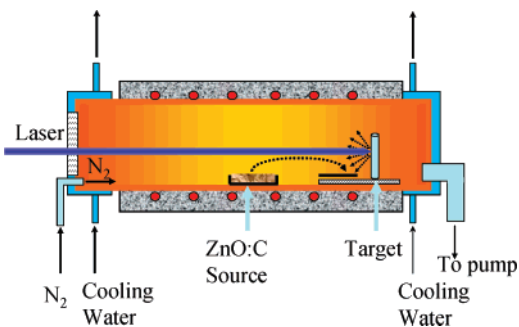


Figure 1. Schematic setup of the thermal-assisted PLD system. A pressed $\text{Zn}_3\text{P}_2/\text{ZnO}/\text{Zn}$ target is ablated with an excimer laser, and ZnO/C source materials are in the middle. Vapors are released and recondensed as Zn_3P_2 nanostructures on the target and substrate.

mbar and held for 2–3 h before the introduction of N_2 and maintained at a constant pressure of 200 mbar thereafter. The furnace was then heated up at a rate of $50\text{ }^\circ\text{C}/\text{min}$ to the desired peak temperature of $1100\text{ }^\circ\text{C}$ and held for another 20 min before slowly cooling down. Once the temperature exceeded $900\text{ }^\circ\text{C}$, a Compendex Series Excimer 102 laser (248 nm, 10 Hz, 30 kV, $\sim 300\text{ mJ}$) started to generate pulsed laser energy and kept shining a laser spot, 1 mm wide and 5 mm long, on the target during the synthesis until the furnace was cooled down to $900\text{ }^\circ\text{C}$.

When the synthesis process was completed, dark yellowish fuzzy material was found around the laser ablated pit on the target and on the surface of the substrate. The morphology of the as synthesized materials was examined using a LEO 1530 field emission scanning electron microscope (SEM) and the composition of Zn and P was first confirmed with energy dispersive spectrometry (EDS) attached to SEM.

Figure 2 shows typical SEM images of the as synthesized Zn_3P_2 nanostructures and analysis results using EDS and XRD. A top view of the as synthesized nanostructures on a Si substrate is present in Figure 2a and its inset, which shows that those hierarchical nanostructures take a 6-fold symmetry. The tree shape is further revealed in the side view of Zn_3P_2 nanostructures in Figure 2b, which is the as synthesized product from the target lying on a conductive carbon tape for SEM imaging. The constituent branches of those tree-shape structures can be as long as several tens of micrometers. The diameter of those branches is in the range of 10 nm to a few hundred nm. Generally the branches at the root of the central trunk are larger than those at the top part of the trunk. A single branch is uniform and gradually gets smaller toward its tip. When the branches grow longer, some Zn_3P_2 nanobelts are also formed, as shown in Figure 2c. The thickness is in the range of 100 nm to several hundred nm, but the same nanobelt has a very uniform thickness throughout the entire belt. In comparison, the widths vary dramatically, even within a single nanobelt. As can be seen from Figure 2c, some nanobelts can be as wide as $10\text{ }\mu\text{m}$ at the root and get noticeably narrower toward the tip. Smaller nanobelts have also been observed, as shown in the inset in Figure 2c with a width around 100 nm. Considering their superlong length, those nanobelts are still overall very uniform. Besides those hierarchical nanostructures and

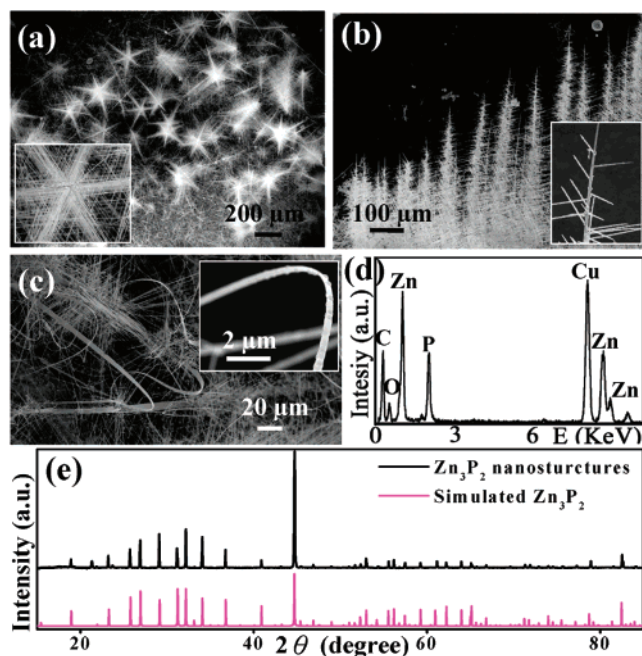


Figure 2. SEM, EDS, and XRD analysis of Zn_3P_2 nanostructures. (a) Low magnification SEM image and an enlarged one of the as grown Zn_3P_2 nanostructures on Si substrate, showing 6-fold symmetry. (b) SEM image of the side view of tree-shaped nanostructures from target with an enlarged part in the inset. (c) SEM images of belt-shaped Zn_3P_2 . (d) EDS indicating the chemical signature of grown nanostructures. (e) XRD data show a single phase of tetragonal structured Zn_3P_2 with the red line displaying a simulated spectrum for the standard Zn_3P_2 powder.

derivative nanobelts, numerous Zn_3P_2 nanowires (NWs) with diameters up to 100 nm have also been found on the surface of the Si substrates. EDS analysis in both SEM and transmission electron microscopy (TEM) modes gave the same result for all nanostructures reported in this paper, including tree-shaped nanostructures, nanowires, and nanobelts. A typical spectrum in Figure 2d, which was taken from a Zn_3P_2 branch during TEM analysis, indicates the presence of Zn and P from the nanostructure, with Cu and C peaks originating from the sample grid, and O peaks from contamination during the sample preparation or from partial oxidation of the nanostructure.

X-ray diffraction characterization in Figure 2e, performed using a PANalytical X-Pert Pro MRD with $\text{Cu K}\alpha$ radiation, confirms that the phase of the nanostructures is tetragonal Zn_3P_2 (JCPDS Card No. 65-2854) with lattice constants $a = 8.095\text{ }\text{\AA}$ and $c = 11.47\text{ }\text{\AA}$. XRD analysis indicates that the synthesized nanostructures are single-phased Zn_3P_2 with very good crystallinity. No Zn, ZnO , or any other phases are detectable.

Zn_3P_2 nanostructures were further examined using a Hitachi HF-2000 (FEG) transmission electron microscope, as shown in Figure 3. Figure 3a presents a TEM image of a part of a Zn_3P_2 nanostructure with selected area electron diffraction (SAED) patterns recorded from the circled areas labeled b–g and shown in Figure 3b–g, respectively. All of the branches in Figure 3a are in the same plane, and the angle between them is about 60° . As expected, all of the SAED patterns from different locations are along the same

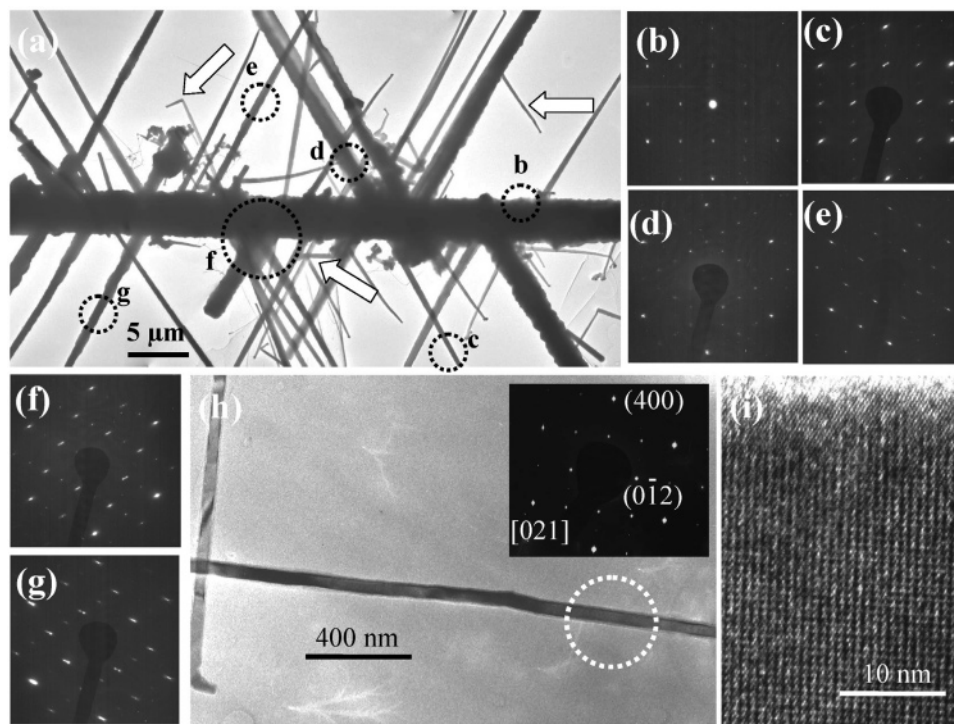
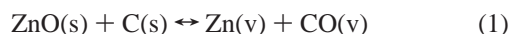


Figure 3. A detailed crystal structure analysis with TEM. (a) Low-magnification TEM image of Zn_3P_2 structure with SAED patterns from circled areas labeled b–g and shown in panels b–g, respectively. The arrowheads indicate secondary branch growth. (h) TEM image of Zn_3P_2 nanowires with SAED from the circled area and (i) a high-resolution TEM image.

zone axis, [021]. Additionally, in-plane rotations are found for some of the SAED patterns, indicating the existence of twin structures when forming the branches. More detailed analysis will be reported separately. Figure 3h present a TEM image of a Zn_3P_2 nanobelt with the same SAED as that of nanostructures in Figure 3a, which is reasonable because nanobelts always grow from those nanostructures, based on SEM observation. According to those SAED patterns, we conclude that the central wire in Figure 3a and the nanobelts in Figure 3h have a growth front of $(0\bar{1}2)$. The top and bottom branches in Figure 3a have growth fronts of $(3\bar{1}2)$, $(31\bar{2})$, or the opposite directions. Secondary branches can also grow from grown branches, as indicated by arrowheads in Figure 3a. The high-resolution TEM image in Figure 3i taken from the circled area in Figure 3h illustrated the nearly perfect single-crystalline arrangement of atoms in the nanowires. Amorphous materials are scarcely seen on the surface. In addition, no ZnO layer has ever been seen on the surface of those Zn_3P_2 nanostructures. Electron microscopy and XRD data demonstrate that perfectly crystalline Zn_3P_2 nanostructures free from an oxidization layer can be obtained. Because no catalyst was introduced during the synthesis and no catalyst was found at the tip or bottom of the grown nanostructures, the nanostructures were formed by a vapor–solid (VS) process. The ZnO and graphite in the middle of the tube follow a carbon-thermal evaporation process as follows¹⁷



Zn vapor was transferred by N_2 carrying gas downward to the reaction area around the target. Being a mixture of

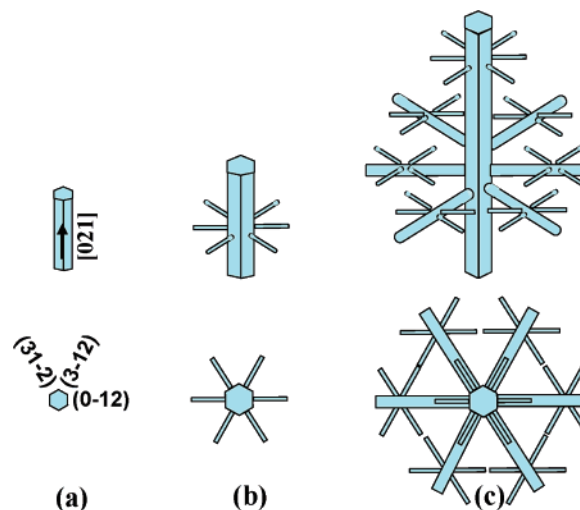


Figure 4. (a) Growth of a Zn_3P_2 nanowire along [021]. (b) Branch growth from the central wire. (c) Formation of tree-shaped Zn_3P_2 nanostructure as a result of continuous growth of side branches and secondary branches.

Zn_3P_2 , ZnO, and Zn, the target releases vapors mainly composed of Zn, P, and O ions under the laser ablation that provides enough energy to break the Zn–P and Zn–O bonds. The O ions were mainly taken by oxidizing the carbon and CO, making it possible for the Zn and P ions to join, resulting in the growth of Zn_3P_2 nanowires. The Zn_3P_2 wires grow along [021] and later are followed by the growth of side branches, as shown schematically in Figure 4. Figure 4a illustrates a Zn_3P_2 wire along [021] with three sets of side surfaces $(0\bar{1}2)$, $(3\bar{1}2)$, and $(31\bar{2})$. A continuous supply of Zn and P results in the growth of the side branches from the

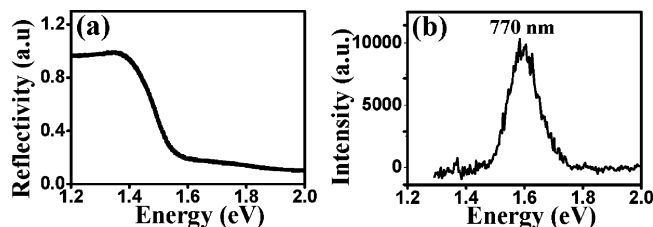


Figure 5. (a) Reflection spectrum of Zn_3P_2 nanostructures. (b) The corresponding photoluminescence spectrum.

central wire, as shown in Figure 4b. The side growth with 6-fold symmetry results from the fact that the angles between the side surfaces in Figure 4a are 120° . When the central wire and the side branches grow longer, new branches will grow from the central wire and even secondary branches also grow from the side branches, which is illustrated in Figure 4c and can be found in Figure 2a.

The optical performance of Zn_3P_2 nanostructures is very interesting. Figure 5 shows a reflection spectrum from 1 to 2 eV (Figure 5(a)) and photoluminescence (PL) spectrum under the excitation of 326 nm at room temperature (Figure 5(b)). From the reflectance spectrum it can be seen that energies below 1.4 eV are almost totally reflected by the Zn_3P_2 nanostructures without absorption, while a distinct edge was found at approximately 1.4 eV, indicating a strong absorption of higher energies.¹⁸ The corresponding PL spectrum provides direct evidence of this distinct absorption edge, at which a broad peak of 1.4–1.7 eV can be found. The broad spectrum found in PL likely results from the free exciton emission near the band edge, namely, acceptor-bound excitons.¹⁹

In addition, single Zn_3P_2 nanostructures were prepared for the investigation of photoconductivity under the illumination of different wavelengths of light or a white LED lamp, as shown in Figure 6a. To characterize the I – V characteristics of single NW, we placed a Zn_3P_2 NW between two Au electrodes via a dielectrophoresis (DEP) technique and deposited Pt by focused ion beam (FIB) microscopy as the top electrode to improve the contact. An ohmic contact can be obtained between Au and Zn_3P_2 .²⁰ In addition, Pt/ Zn_3P_2 also forms an Ohmic contact because Pt has a greater work function (5.7 eV) than p-type Zn_3P_2 (5.06 eV) despite the possible presence of Ga dopants during the Pt deposition process. The ohmic contact was also proved by the linear behavior in later I – V measurement of the device. The representative nanodevice is schematically illustrated in the upper inset of Figure 6a and the corresponding SEM image of the nanodevice is inset in Figure 6a. A LabView program was used to control the two-terminal I – V testing process. The linear I – V characteristic without illumination of light (blue line) confirms the ohmic contact between the electrodes and Zn_3P_2 NW, and a resistance about $3.63 \times 10^9 \Omega$ is derived. The resistivity of Zn_3P_2 NW was calculated about $5.6 \times 10^2 \Omega \text{ cm}$ with the length and the diameter as $35 \mu\text{m}$ and 232 nm , respectively, based on the SEM characterization. The dark resistance here is higher than that of its thin film counterpart (2 – 3×10^2)²¹ possibly due to the contact resistance. On the other hand, under the illumination of light

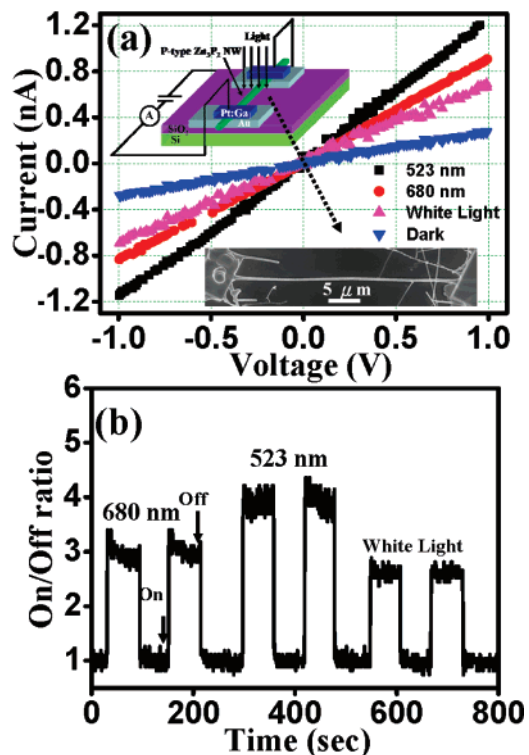


Figure 6. (a) I – V curve for a single Zn_3P_2 NW in the dark or under illumination of different wavelengths of light. Upper inset shows the device configuration under the illumination of light. Bottom inset shows the corresponding SEM image of the Zn_3P_2 NW based nanodevice. (b) On/off ratio as a function of the time under red (680 nm), green (523 nm), or white light illumination, respectively.

at a wavelength of 532 nm (green color with power $< 5 \text{ mW}$), 680 nm (red color with power $< 5 \text{ mW}$), or continuous wavelength from a white LED lamp, the resistance decreased significantly due to excess electron–hole pairs (EHPs) excited by the illuminating light, which has an energy larger than the band gap of Zn_3P_2 . In addition, the desorption of the contaminants from the surface due to the illumination increased the conductivity as well. It is reasonable to expect that the shorter wavelength results in higher photoconductivity because the light with higher energy can create more electron–hole pairs inside the NW. In addition, the excess energy ($h\nu - E_g$) created phonons in the lattice and raised the temperature, resulting in larger electron and hole mobility and contributing a higher conductivity. The on/off ratio, which is defined as the current under the illumination over the dark current, is presented in Figure 6b as a function of the illuminated time, indicating high sensitivity of Zn_3P_2 NW to the illumination of different wavelength of light. The response time for all of the light is considerably less than 1 s with the on/off ratio being about 3 for red light (680 nm), 4–5 for green light (532 nm), and 2–3 for white light from a LED lamp.

Having shorter response time and higher on/off ratio than that of single NW,²² the p–n photodiode is an alternative form of photoconductor and can be constructed with crossed nanowires.^{23,24} By combination with wide band gap materials, such as ZnO, SnO_2 , and ZnS, the whole range of light from

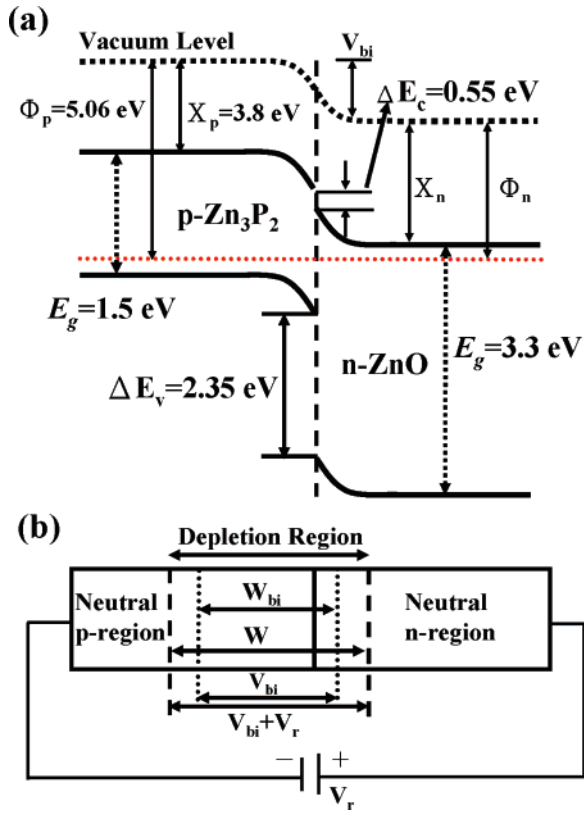


Figure 7. (a) The ideal energy diagram for ZnO/Zn₃P₂ heterojunction. (b) The individual position and length for neutral n- and p-regions as well as the depletion region without applied bias and under reverse bias, respectively.

ultraviolet to the near-infrared can be effectively absorbed by this kind of photodiode, which is beneficial for terrestrial application of solar cell. We report the performance of a prototype nanoscale photodiode based on the crossed structure of a p-type Zn₃P₂ NW with an n-type ZnO NW. In order to form the required nano-heterojunction, we aligned a Zn₃P₂ NW between two Au electrodes via the DEP technique and fixed it with Pt metal via a FIB, which can improve the contact. After that, a ZnO NW was aligned perpendicular to Zn₃P₂ NW by DEP technique and connected to another pair of Au electrodes via Pt deposition by FIB microscopy. The final structure and schematic diagram are illustrated in insets of Figure 8a. The composition of the two NWs is confirmed with EDS and an ohmic contact is achieved individually for both ZnO and Zn₃P₂ (please see the Supporting Information, Figures S1a–d). In order to further understand the detailed issue of this nano-heterojunction, an ideal energy diagram of this heterojunction is constructed in Figure 7a on the basis of the experimental data. According to the band gap E_g (3.3 eV for ZnO and 1.5 eV for Zn₃P₂) and electron affinity X (4.35 eV for ZnO and 3.8 eV for Zn₃P₂), the ZnO/Zn₃P₂ heterojunction exhibits a type II (staggered) alignment. The energy barrier for electrons, ΔE_c , is found about 0.55 eV via $\Delta E_c = X_{\text{ZnO}} - X_{\text{Zn}_3\text{P}_2}$. Meanwhile, the energy barrier for holes, ΔE_v , is found to be 2.35 eV via $\Delta E_v = E_{g,\text{ZnO}} + \Delta E_c - E_{g,\text{Zn}_3\text{P}_2}$. Accordingly, ΔE_c is smaller than ΔE_v , causing electron injection from n-type ZnO to p-type Zn₃P₂ to be more favorable than hole injection from p-type Zn₃P₂ to

n-type ZnO. The resultant neutral p-region, neutral n-region, and the depletion region in the absence of applied bias are shown in Figure 7b with the length of the depletion region and built-in voltage defined as W_{bi} and V_{bi} , respectively. In addition, it is well-known that the carrier concentration of ZnO NW is found in the range of $\sim 10^{17} - 10^{18} \text{ cm}^{-3}$,²⁵ which is consistent with the bulk counterpart. In contrast, the carrier concentration of Zn₃P₂ NW has not been reported in the literature. If we make the hypothesis that the carrier concentration of Zn₃P₂ NW is the same order as that for thin films and on the order of $\sim 10^{15} \text{ cm}^{-3}$, the ZnO/Zn₃P₂ nano-heterojunction can be considered as an abrupt N⁺P junction, in which the depletion region is almost located at the Zn₃P₂ side, which have been calculated for the thin film case.⁸ The N⁺P junction characteristic is revealed by the rectification behavior of the I – V measurement in Figure 8a. At high forward bias, some of the minority carriers can diffuse and recombine in the depletion region, resulting in the recombination current. Considering the contribution of diffusion and recombination currents under forward bias, a simple I – V behavior can be empirically given by^{26,27}

$$J \approx J_0 \exp\left(\frac{eV}{nkT}\right) \quad (2)$$

where J_0 is the saturated current, n is an ideality factor, k is Boltzmann's constant, and T is the absolute temperature, respectively. When the I – V curve is dominated by an ideal diffusion current, $n = 1$; whereas when the I – V curve is dominated by a recombination current, $n = 2$. Otherwise, when n has a value between 1 and 2, both mechanisms are at play. However, the ideality factor $n > 2$ is received in the present study by fitting the plot of $\ln(J/J_0)$ as a function of forward bias, which likely results from the high contact resistance at both the interfaces of (Pt, Au)/ZnO NW and (Au, Pt)/Zn₃P₂ NW and is consistent with previous reports.²⁷ In order to distinctly display the I – V behavior of the photodiode under the illumination of different wavelength lights, we reversed the polarity of the input voltage compared with the one in Figure 8a. The I – V curves for the photodiode under reverse bias and in the dark and under the illumination of light with wavelength of 532 or 680 nm are presented in Figure 8b, showing apparent current enhancement by the light. The increase of the current results from the generation of electron–hole pairs inside the depletion region and nearby under the excitation of the light and can be given by

$$I_{ph} = I_n + I_p = q\Delta n v_n + q\Delta p v_p \quad (3)$$

where I_{ph} is the total photocurrent density, I_n and I_p are the photocurrents caused by electrons and holes. q , Δn , Δp , v_n , and v_p represent electronic charge, the concentration of generated electrons and holes, and average drift velocities of electrons and holes within the specific depletion field, respectively. The concentration of the generated electron–hole pairs and the resultant current as well increase with the increase of the energy and intensity of incoming light, which explains why red light causes less current enhancement than

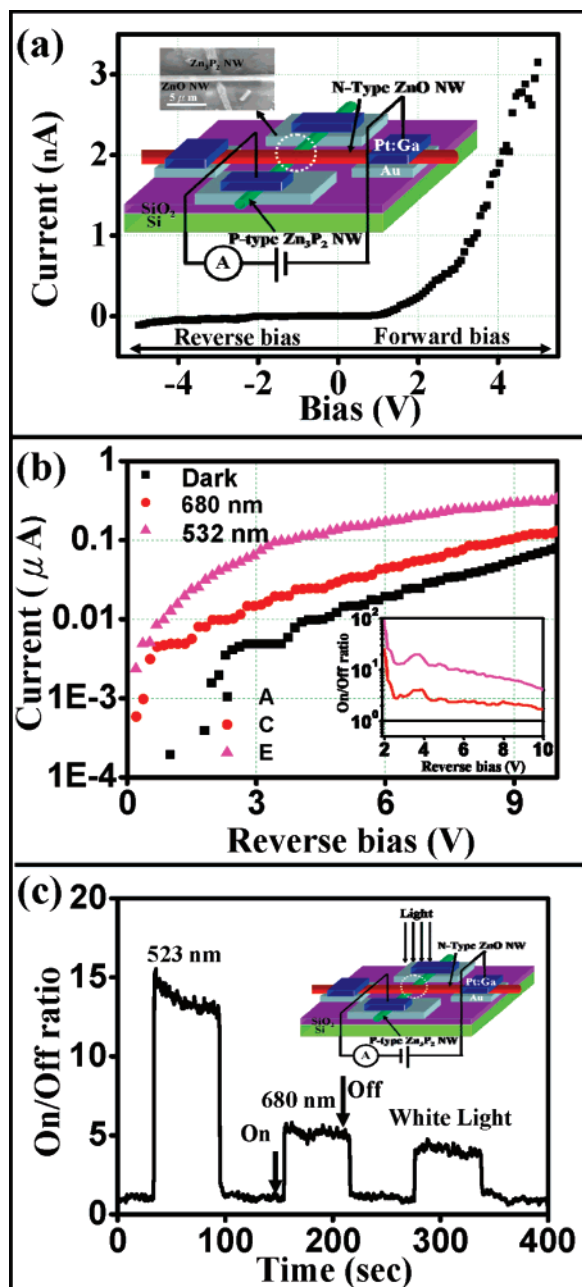


Figure 8. (a) I – V curve for ZnO/Zn₃P₂ nanoscale heterojunction at reverse and forward bias. Inset shows the prototype of the nanodevice, in which a ZnO NW was placed on top of a Zn₃P₂ NW. (b) I – V curve of ZnO/Zn₃P₂ heterojunction under illumination of different wavelengths as displayed in logarithmic scale under reverse bias. (c) The on/off ratio as a function of the time under red (680 nm), green (523 nm), or white light illumination, respectively. The inset is the schematic of the device.

green light while the dim white light produces the least enhancement. In addition, the lights have greater effect on reverse biased photodiode than forward biased photodiode, which is consistent with the fact that the photoexcited electron–hole pairs can significantly influence the concentration of minority carriers, which dominate the current through a reverse biased diode. The influence of the lights on the reverse biased photodiode is illustrated explicitly in Figure 8b with logarithmic scale and with the on/off ratio plot shown inset. Interestingly, all of the current from the

illumination of light shows a similar trend: significantly greater than dark current under low reverse bias and more and more comparable to dark current under higher reverse bias.

In general, the reverse current is composed of the diffusion current in neutral regions and the generation current in the depletion regions. The reverse current, or reverse saturation current, comes from minority carriers in the neutral region, which diffuse toward and subsequent drift through the depletion region. On the other hand, the generation current comes from electron–hole pairs which are generated in the depletion region and drift toward neutral regions under the internal field. Thermal generated minority carriers and electron–hole pairs contribute to the dark current. In contrast, the impinging photon can generate substantial electron–hole pairs in both the depletion region and neutral region on the Zn₃P₂ side and considerably enhance the reverse current. At low reverse bias, photon-generated carriers are overwhelming over thermal generated carriers and result in a surprisingly high on/off ratio ($\sim 10^2$) in the inset of Figure 8b. However, thermal generated electron–hole pairs increase with increased bias and contribute more and more to the reverse current, as can also be seen in the dark current curve in Figure 8a. Accordingly, the on/off ratio should decrease with increased reverse bias, which confidently agrees with our result in the inset of Figure 8b. Despite of the decrease at high reverse bias, the on/off ratio can still reach 9–10, which is superior to other single NWs as photoconductors.^{28–31}

Additionally, the photon response of the photodiode to different lights is shown in Figure 8c in which we applied a fixed reverse bias of 5 V and turned on and off green light (523 nm), red light (680 nm), and the white light lamp serially. Green light produces the highest (~ 13) on/off ratio as expected. Interestingly, the dim white light also produces an on/off ratio (~ 5) which is significantly greater than 1, indicating the high sensitivity of the photodiode to visible lights. Furthermore, the response time for all tested lights is below 1 s. The very nice performance of the diode may result from the following advantages. First of all, the top ZnO NW has a wide band gap and the light from infrared to violet can penetrate easily with minimum energy loss.^{32,33} Second, the depletion region is mostly located at the Zn₃P₂ NW side so that electron–hole pairs can be generated by a wide light range from 380 to 800 nm, and significant generation current enhancement results. Finally, the large minority diffusion length of Zn₃P₂ enables more photon-generated minority carriers in the neutral region to diffuse into the depletion region and results in a large on/off ratio and high sensitivity as well. The high sensitivity, quick response, and nanoscale size can benefit the ZnO/Zn₃P₂ nanoscale heterojunction as a candidate for a high efficient and spatial resolved photon detector.

In summary, we have synthesized tree-shaped Zn₃P₂ nanostructures, nanobelts, and nanowires in a thermal-assisted laser ablation process and proposed a possible growth process of those nanostructures. The photoluminescence spectrum of Zn₃P₂ nanostructures shows a broad emission centered at 770 nm with a slight blue shift with regard to that of the

bulk Zn₃P₂. A strong absorption from ultraviolet to near-infrared is apparent from the reflectivity measurement of those nanostructures. Taking advantage of the direct band gap of 1.5 eV, high absorption coefficient, large minority diffusion length, and high crystallinity free from oxidization, those nanostructures have potential applications in solar cell, broad range photodetectors, lasers, etc. Preliminary investigation on their application has been performed on the optoelectric measurement of a single Zn₃P₂ nanowire and a nanoscale photodiode.

The conductance of a single Zn₃P₂ nanowire shows high sensitivity to green light (523 nm), red light (680 nm), and white light and is very suitable as a photoconductor. Furthermore, we also constructed a nanoscale photodiode with crossed ZnO/Zn₃P₂ nanowires. The linear behavior of individual nanowires and the rectification behavior between ZnO and Zn₃P₂ revealed the formation of p–n heterojunction. Despite the absence of an antireflection coating or any other optimization, the photon diode gives rapid response and very high on/off ratio upon the illumination of light. Considering their small size, we expect Zn₃P₂ nanostructures and corresponding heterojunctions will play an important role in nano-optoelectronics.

Acknowledgment. Support from NASA Vehicle Systems, Department of Defense Research and Engineering (DDR&E), the Defense Advanced Research Projects Agency (Award No. N66001-04-1-8903), and CCNE from NIH is gratefully acknowledged. Y.U.C. is grateful for the support of the Thousand Horse Program No. 095-2917-1-007-014.

Supporting Information Available: EDS data and *I*–*V* measurement of individual constituent nanowires of the heterojunction. This material is available free of charge via the Internet at <http://pubs.acs.org>.

References

- Fessenden, R. W.; Sobhanadri, J.; Subramanian, V. *Thin Solid Films* **1995**, *266*, 176–181.
- Kakishita, K.; Aihara, K.; Suda, T. *Appl. Surf. Sci.* **1994**, *80*, 281–286.
- Misiewicz, J.; Bryja, L.; Jezierski, K.; Szatkowski, J.; Mirowska, N.; Gumienny, Z.; Placzekpopko, E. *Microelectron. J.* **1994**, *25*, R23–R28.
- Park, M. H.; Wang, L. C.; Cheng, J. Y.; Deng, F.; Lau, S. S.; Palmstrom, C. J. *Appl. Phys. Lett.* **1996**, *68*, 952–954.
- Hava, S. J. *Appl. Phys.* **1995**, *78*, 2808–2810.
- Kakishita, K.; Aihara, K.; Suda, T. *Sol. Energy Mater.* **1994**, *35*, 333–340.
- Suda, T. *J. Cryst. Growth* **1990**, *99*, 625–629.
- Nayar, P. S. *J. Appl. Phys.* **1982**, *53*, 1069–1075.
- Weller, H.; Fojtik, A.; Henglein, A. *Chem. Phys. Lett.* **1985**, *117*, 485–488.
- Green, M.; O'Brien, P. *Chem. Mater.* **2001**, *13*, 4500–4505.
- Buhro, W. E. *Polyhedron* **1994**, *13*, 1131–1148.
- Shen, G. Z.; Bando, Y.; Hu, J. Q.; Golberg, D. *Appl. Phys. Lett.* **2006**, *88*, 143105.
- Wang, Z. L. *J. Phys.: Condens. Matter* **2004**, *16*, R829–R858.
- Ganesan, P. G.; McGuire, K.; Kim, H.; Gothard, N.; Mohan, S.; Rao, A. M.; Ramanath, G. *J. Nanosci. Nanotechnol.* **2005**, *5*, 1125–1129.
- Liu, Z. Q.; Zhang, D. H.; Han, S.; Li, C.; Tang, T.; Jin, W.; Liu, X. L.; Lei, B.; Zhou, C. W. *Adv. Mater.* **2003**, *15*, 1754–1757.
- Morber, J. R.; Ding, Y.; Haluska, M. S.; Li, Y.; Liu, P.; Wang, Z. L.; Snyder, R. L. *J. Phys. Chem. B* **2006**, *110*, 21672–21679.
- Song, J. H.; Wang, X. D.; Riedo, E.; Wang, Z. L. *J. Phys. Chem. B* **2005**, *109*, 9869–9872.
- Bryja, L.; Jezierski, K.; Misiewicz, J. *Thin Solid Films* **1993**, *229*, 11–13.
- Fuke, S.; Kawarabayashi, S.; Kuwahara, K.; Imai, T. *J. Appl. Phys.* **1986**, *60*, 2368–2371.
- Babu, V. S.; Vaya, P. R.; Sobhanadri, J. *Semicond. Sci. Technol.* **1989**, *4*, 521–525.
- Kakishita, K.; Ikeda, S.; Suda, T. *J. Cryst. Growth* **1991**, *115*, 793–797.
- Sze, S. M. *Physics of Semiconductor Devices*; Wiley: New York, 1981.
- Duan, X. F.; Huang, Y.; Cui, Y.; Wang, J. F.; Lieber, C. M. *Nature* **2001**, *409*, 66–69.
- Zhong, Z. H.; Qian, F.; Wang, D. L.; Lieber, C. M. *Nano Lett.* **2003**, *3*, 343–346.
- Fan, Z. Y.; Wang, D. W.; Chang, P. C.; Tseng, W. Y.; Lu, J. G. *Appl. Phys. Lett.* **2004**, *85*, 5923–5925.
- Kasap, S. O. *Principles of Electronic Materials and Devices*, 2nd ed.; McGraw-Hill: NY, 2002.
- Wang, C. X.; Yang, G. W.; Liu, H. W.; Han, Y. H.; Luo, J. F.; Gao, C. X.; Zou, G. T. *Appl. Phys. Lett.* **2004**, *84*, 2427–2429.
- Philipose, U.; Ruda, H. E.; Shik, A.; de Souza, C. F.; Sun, P. J. *Appl. Phys.* **2006**, *99*, 066106.
- Law, J. B. K.; Thong, J. T. L. *Appl. Phys. Lett.* **2006**, *88*, 133114.
- Mathur, S.; Barth, S.; Shen, H.; Pyun, J. C.; Werner, U. *Small* **2005**, *1*, 713–717.
- Kim, K.; Kim, B. H.; Joo, S. H.; Park, J. S.; Joo, J.; Jin, J. I. *Adv. Mater.* **2005**, *17*, 464–468.
- Park, C. H.; Jeong, I. S.; Kim, J. H.; Im, S. *Appl. Phys. Lett.* **2003**, *82*, 3973–3975.
- Ma, J.; Ji, F.; Ma, H. L.; Li, S. Y. *Thin Solid Films* **1996**, *279*, 213–215.

NL062228B